Beam Performance

Developments and Upgrades of Storage Ring and Booster Synchrotron

Improvement of the Coupling Correction

The vertical beam spread is one of the most important parameters for the high brilliance storage ring, which is represented by the coupling ratio of the horizontal and vertical beam emittances. The coupling between the horizontal and vertical betatron oscillations and the vertical dispersion with the energy spread generate the vertical beam spread, so that they should be corrected. The latter has been corrected since 1999, and the former since 2007, both of which are controlled using skew quadrupole magnets [1-3].

The betatron coupling has an effect on the beam through the resonance of the beam motion. The coupling has sum and difference resonances that form the lattice on the tune map, as shown in Fig. 1. In the early stage of the coupling correction, only the nearest neighbor resonance ($\nu_x - \nu_y = 22$) to the operation point (40.15, 18.35) was corrected. At present, to improve the correction, four resonances surrounding the operation point are corrected.

From the perturbation theory of the betatron motion with the single resonance approximation [4,5], it is implied that the vertical beam size is proportional to the strength of the coupling resonance. Hence, the strengths of the skew quadrupole magnets for the coupling correction are determined so as to give the minimum vertical beam size. Resonance modes are orthogonal to each other, so that they are corrected independently by the appropriate combination of skew quadrupole magnets. Moreover, although the strength of the coupling resonance is a complex value and has two degrees of freedom, it is corrected independently with a sufficient number of skew quadrupole magnets. The tuning process of the coupling correction is shown in Fig. 2. The fitting curves obtained with the quadratic approximations represent the changes in the vertical beam size with respect to the strengths of the coupling resonances in terms of the skew quadrupole magnets. The light blue crossing symbols joined by the straight lines represent the minimum vertical beam size in each tuning process of the coupling resonances. The more the modes of the coupling resonances are corrected, the smaller the vertical beam size becomes.

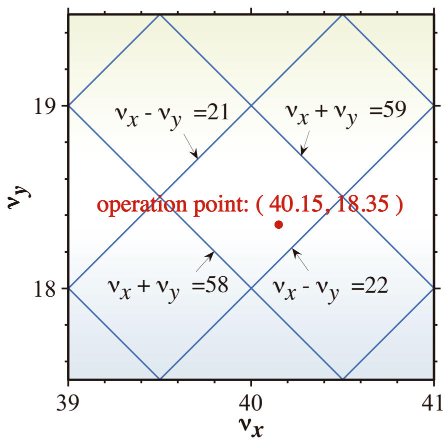

Fig. 1. Coupling resonances around the operation point in the SPring-8 storage ring.

In tuning of the emittance coupling, the vertical dispersion correction is performed after the betatron coupling resonance correction. This is because the former correction can be performed without exciting the coupling resonances. As a result of these corrections, we achieve the emittance coupling ratio of 0.2%.

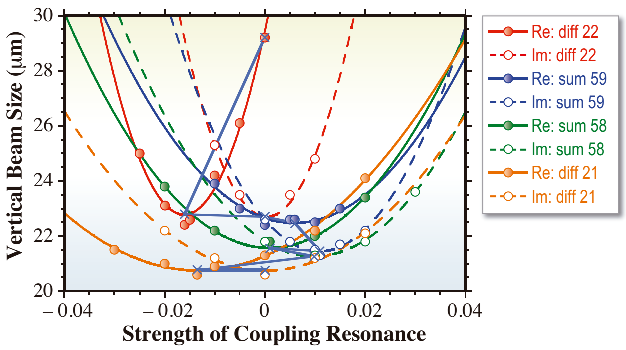

Fig. 2. Tuning of the coupling correction.

Lattice Modification for Installing Small-Gap Undulators in the Long Straight Section

There are four magnet-free long straight sections of about 30 m in the SPring-8 storage ring. In two of these sections, a 25-m-long undulator (BL19LXU) and a series of figure-8 undulators (BL07LSU) have already been installed. In addition, a set of short-period undulators with a narrow gap is planned to be installed in one of the remaining long straight sections to build a high performance beamline for inelastic X-ray scattering (BL43LXU). To obtain sufficient photon flux and brilliance over a desired energy range, it is necessary to make the minimum undulator gap as small as possible.

To this end, we designed a new lattice (Fig. 3) in which one of the long straight sections is divided into three sub-sections for installing three 5-m-long undulators and the rest of the ring is kept unchanged. Additional quadrupole magnets will be installed between the sub-sections to lower the vertical betatron function, and hence, allow smaller undulator gaps. The vertical betatron function takes the minimum value of 5.0 m at the middle of each sub-section, and the allowable minimum gap of undulators is 5.2 mm that is obtained by scaling the currently allowed minimum gap at other straight sections.

In the new lattice, however, the symmetry of the ring is lowered, and in general, in such a ring with low symmetry, it becomes difficult to maintain a sufficient dynamic aperture for on- and off-momentum electrons. If the dynamic aperture shrinks, the injection efficiency and beam lifetime are largely affected. To avoid this and keep the dynamic aperture large, we extended the method of "quasi-transparent matching of sextupole fields" [6] by incorporating the concept of "counter-sextupoles" [7] and applied it. With this new technique, we could recover the dynamic aperture even after breaking the lattice symmetry as shown in Fig. 4: we kept the betatron phase condition for transparent matching of optics, carried out local chromaticity correction for off-momentum electrons and reduced the dominant effect of nonlinear kicks using sextupole magnets in the matching section. Commissioning of the new beamline is planned in the second half of 2011, and accelerator components (magnets, vacuum chambers, girders, new power supplies, etc.) will be rearranged and settled in accordance with the schedule.

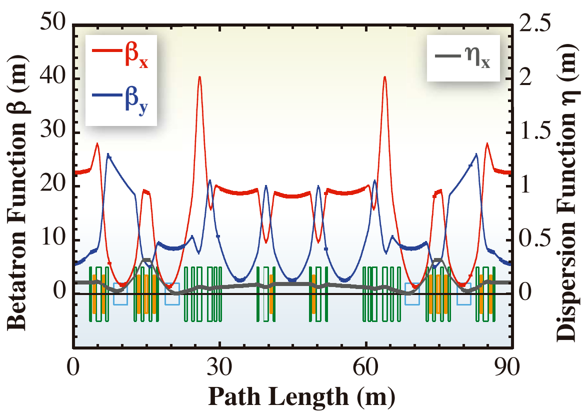

Fig. 3. Newly designed lattice functions for the modified long straight section for BL43LXU. The horizontal betatron function (β_x), vertical betatron function (β_y), and horizontal dispersion function (η_x) are shown. Also shown in the figure is the magnet arrangement (blue: bending magnets, green: quadrupole magnets, orange: sextupole magnets).

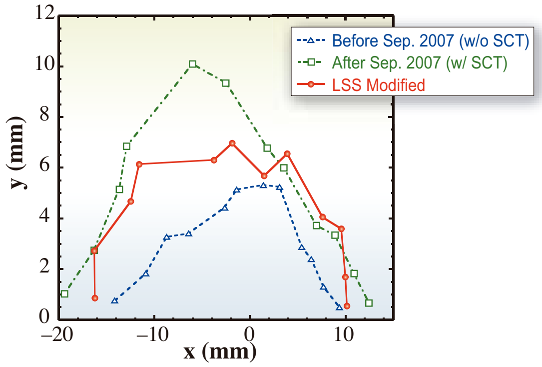

Fig. 4. Comparison of dynamic aperture simulations. The dashed line (blue) is for the ring without counter-sextupole magnets before September 2007, the dot-dashed line (green) is for the ring with counter-sextupole magnets after September 2007, and the solid line (red) is for the ring with a locally modified long straight section as shown in Fig. 3.

Suppression of Stored Beam Oscillation at Injection

In top-up operation, it is important that frequent beam injections should not affect the stored beam. At the time of beam injection, a pulsed bump orbit is made using four bump magnets. This bump orbit is not closed perfectly, and as a result, the horizontal oscillation of a stored beam is excited. To stabilize the photon beam axis during injection, we have been trying to suppress the oscillation amplitude by improving the bump magnet design, reducing the effect due to the nonlinearity of sextupole magnets, tuning circuits of bump magnet power supplies, introducing a pulsed corrector magnet, etc. With these improvements, the amplitude of residual oscillation in the horizontal direction has now been suppressed well. However, a relatively large oscillation amplitude of about 0.4 mm in RMS remains at the timing of firing bump magnets, which is caused by the non-similarity of the temporal shape of the magnetic field.

From 2007, to suppress this residual oscillation at the timing of firing bump magnets, we started to test a newly developed fast kicker magnet system. We checked its performance with a beam and improved the power supply. A newly developed fast pulsed power supply can generate a current of about 200 A, corresponding to the magnetic field of 4.61 mT, with a pulse width of 1.0 μs. Although this pulse width is slightly broader than required, the kick performance is enough for suppressing the residual oscillation. We then optimized the timing and kick angle to generate the most effective counter kick, and the result is shown in Fig. 5. As seen from the figure, we could suppress the horizontal beam oscillation by about

60% using the kicker magnet system. In the future, we will improve the kicker performance and try to suppress the residual oscillation further.

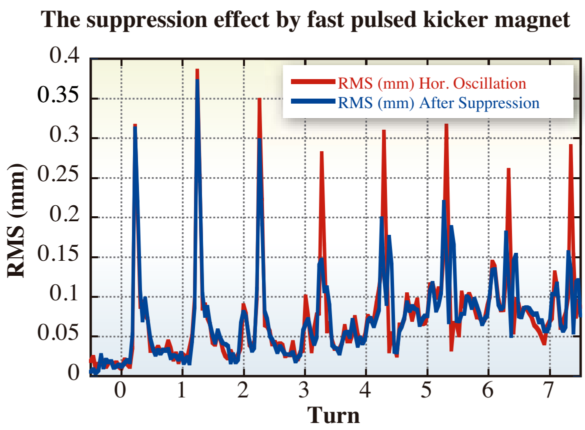

Fig. 5. Suppression of the horizontal beam oscillation using the fast pulsed kicker system. The RMS oscillation amplitude is plotted as a function of the timing (4.8 μs per turn) after the bump firing.

Development of Fast Pulsed Kicker Magnet System

A fast pulsed kicker magnet system can be used to give a vertical kick to the electron bunch and induce the head-tail oscillation for generating short pulsed X-rays [8]. We started developing this system in 2007. The main subject in this development is how to generate large currents with a narrow pulse width using a compact kicker magnet system. The specifications typically required for this system are as follows: current of more than 500 A corresponding to a magnetic field of about 8 mT, pulse width of less than 1 μs, and magnet length of about 0.3 m or shorter.

In constructing the system, we adopted the following as a guiding principle: firstly, we use an air-core type magnet with one-turn coils to lower the inductance as much as possible for fast pulse generation; secondly, we put a power supply system as close as possible to the kicker magnet for the same reason; finally, we separate the driving power supply system from the main high voltage system and put it close to the magnet. Hence, we needed to develop a new compact driving power supply system that should be comparable to the existing 500-A-class large power supply system.

A key technology for this development is the use of a power MOSFET as a switching device. The size of this device is about 2 cm × 2 cm, while the performance is almost the same as that of the IGBT, whose size is larger than that of the MOSFET by a factor of about 20. Using this device, we made the first test system and succeeded in generating 157 A/coil with 2.5 μs pulse width. In 2009, we started developing the second test power supply system and have recently succeeded in generating 270 A/coil with 1.0 μs pulse width. The conceptual design of our compact driving circuit is as follows: a high voltage (max. 900 V) is supplied from the external power supply system, the circuit is turned on by a TTL pulse signal of a trigger amplifier, and the resonant circuit is switched on by four MOSFETs connected in parallel. Figure 6 shows the schematic of the fast pulsed kicker magnet system. The kicker magnet is installed on the ceramic vacuum chamber so as to increase the penetrability of the magnetic field and decrease the eddy current effect and inductance. Figure 7 shows the cross-sectional structure of the kicker magnet and the actually installed kicker magnet system in the storage ring in the case of the vertical kicker. We will continue the development to increase the current up to 500 A and to realize a shorter pulse width of less than 1.0 μs. Results of the application of the fast kicker system can be found in Ref. [9] and elsewhere in this report.

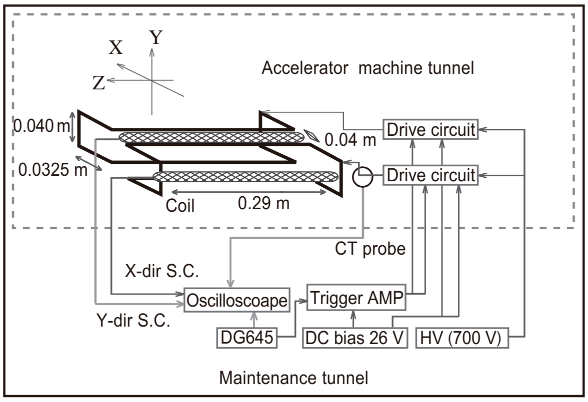

Fig. 6. Schematic of the kicker magnet system (vertical kicker case as an example). A driving circuit is connected to the high voltage power supply and delay generator DG645, and one circuit supplies current to one coil.

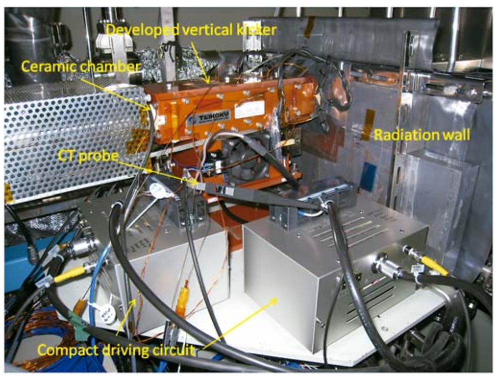

Fig. 7. Photograph of the vertical kicker magnet system installed in the storage ring.

Development of Bunch-by-Bunch Feedback System

The beam instabilities limit the average and bunch current in the SPring-8 storage ring. To overcome these instabilities, digital bunch-by-bunch feedback (BBF) systems were developed and in operation in the storage ring. The BBF is used to detect the position signal of each bunch from a beam position monitor (BPM), calculates the required amount of kick digitally, and drives kickers with bunch-by-bunch bases.

The hybrid filling composed of 10 mA/bunch singlet bunches and a train of bunches with 0.05 mA/bunch has a great advantage to fulfill simultaneously the requirements of both users of high current singlet bunches and of the average current. To achieve such filling, the BBF needs to suppress simultaneously the single-bunch mode-coupling instabilities of the singlet bunches and the coupled-bunch instabilities of the train of bunches. However, the contrast of the bunch current of those bunches is too high for usual BBF systems to control both high and low current bunches without any external devices.

To overcome this problem, we are developing the bunch current sensitive automatic attenuator (BSAT) shown in Fig. 8. The BSAT detects the bunch current and controls the variable attenuators to reduce the level of the BPM position signal of high current bunches to equalize the level of the position signal. Such device is already in operation for the bunch current ratio of six but is insufficient for the high ratio in such hybrid filling. The bench test of the attenuators was performed and satisfactory results in the attenuation and timing performance were obtained. The FPGA program that converts the feedback processor to the controller of the BSAT is under development.

To achieve such hybrid filling, we also need to increase the horizontal kick using the feedback kicker. The horizontal oscillation of the beam is excited by the injection bump formation, and a large kick is necessary to suppress the strong single-bunch instabilities under such large oscillation amplitude. To increase the horizontal kick, we installed the newly developed high efficiency horizontal kicker and confirmed its high efficiency with the beam test, and the kick is increased by a factor of 1.5. The high efficiency kicker also has a vertical kicker inside and its kick is two times more than those of the previous vertical kickers. With this, we could enhance the vertical feedback and could reduce the vertical chromaticity from six to two suppressing the strong beam instabilities in such low chromaticity. This reduction of the chromaticity increased the injection efficiency from ~85% to ~93%, or the beam loss is reduced to half.

In the booster synchrotron, the continuous vertical tune measurement is desired for the stable operation of the bunch purification system based on the RFKO method. However, the usual tune measurement method is not so fast for such application, and thus, we developed a new type of tune measurement system with the feedback shown in Fig. 9. During 100 ms after the injection, this system excites the beam with a positive feedback controlled using the SPring-8 digital

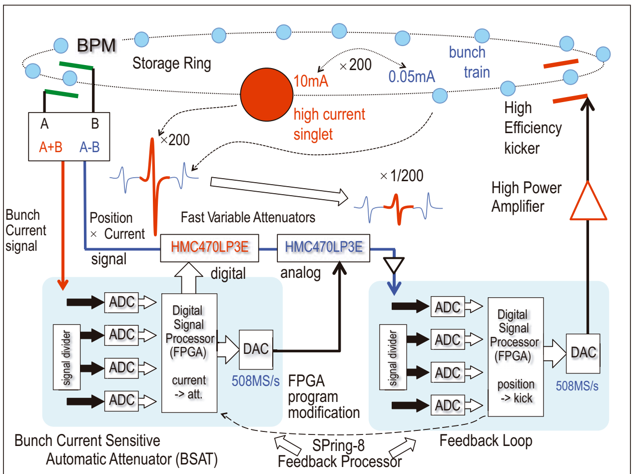

Fig. 8. Bunch current sensitive automatic attenuator (BSAT). The sum signal (A+B) of BPM electrodes (A,B), which is proportional to the bunch current, is detected using a processor based on the SPring-8 feedback processor whose FPGA program is modified for this purpose. The processor calculates the required attenuation and sets variable attenuators (HMC470LP3E and HMC470LP3E). The position signal pulses (A-B) of the bunches are attenuated as its bunch current, and then sent to the feedback processor.

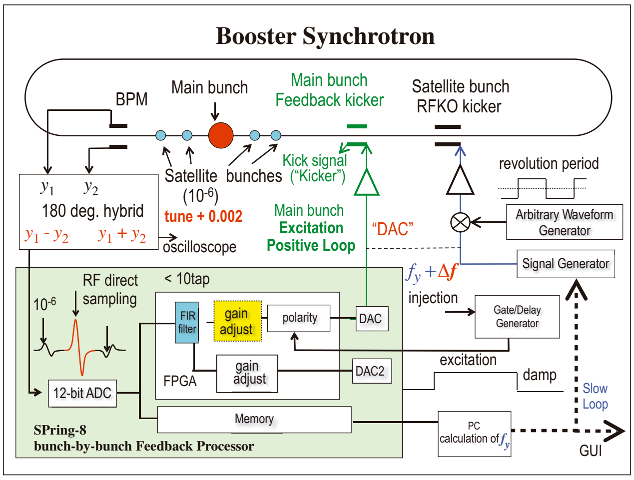

Fig. 9. Continuous tune measurement system for the booster synchrotron of SPring-8. The positive feedback loop by the feedback processor excites the vertical motion of the beam, and the vertical position data is stored in the memory of the processor. These data are sent to a PC to calculate the tune. After the measurement, the polarity of the feedback is inverted and the beam motion is damped. The control of the RFKO frequency (slow loop) based on the measured tune is not yet completed.

feedback processor, and the position data is stored in the memory of the processor for the analysis to find the tune. The beam test of this system was successfully performed.

Improvement of Beam Loss Monitor

By detecting a beam loss in the SPring-8 storage ring, manifesting its mechanism, and handling it, we can suppress irradiation-induced damage to accelerator components and avoid accidents such as vacuum leakage caused by the meltdown of a vacuum chamber [10] and demagnetization of permanent magnets of in-vacuum insertion devices (IDs) [11].

For this purpose, a noise-compensation-type beam loss monitoring system with PIN photodiodes has been developed since Oct. 2008 [12] and installed at characteristic points in the tunnel of the storage ring, such as the injection point, beam dump point, bending magnet of the cell-2 (c2-B2), entrance of the 25-m-long in-vacuum undulator (ID19), the minimum gap height of which is 12 mm, and chamber for the irradiation experiment (SS48).

In Sep. 2009, a common trigger system was introduced to the beam loss monitoring system and additional beam loss detectors were installed. Then, a beam loss distribution around the storage ring has been observed at all times during the user operation. Figure 10 shows the distribution of the beam loss signal on the nominal beam dump and on the beam abort observed from Oct. 28 to Nov. 15. The maximum value of 1.2 V in Fig. 10 indicates the saturation of the signal from the amplifier circuit for the beam loss monitor.

In the case of the nominal beam dump, the largest loss monitor signal is observed around the injection section (i.e., the injection point, dump point, and c2-B2), where a pulsed local bump orbit in the vertical direction is made for slowly scraping the electron beam on the timing of the nominal beam dump. The loss monitor signal is also observed at the out-vacuum IDs (ID05, ID07, and ID08) but not at the in-vacuum IDs (ID09, ID10, ID19, and ID20). It is considered that the secondary particles generated on the nominal beam dump are distributed around the injection section and at the out-vacuum IDs in the storage ring. The beam loss signal at the out-vacuum IDs seems to be related to a trajectory of the electron beam being distorted by the sextupole magnets in the vertical local bump orbit during the nominal beam dump. The mechanism why the beam loss is induced at the out-vacuum IDs on the nominal dump is now under investigation.

In the case of the beam abort, at which the RF accelerating power is suddenly turned off, the beam loss signal is localized at the SS48 and injection point. The signal is not observed at the positions of the IDs. It seems that the chambers at the SS48 and injection point play a key role as the beam scraper. This result is well explained by the tracking simulation using CETRA code (see Fig. 11).

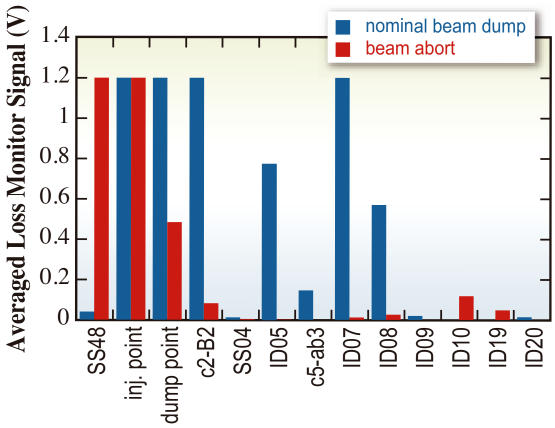

Fig. 10. Distribution of beam loss signal on nominal beam dump and beam abort.

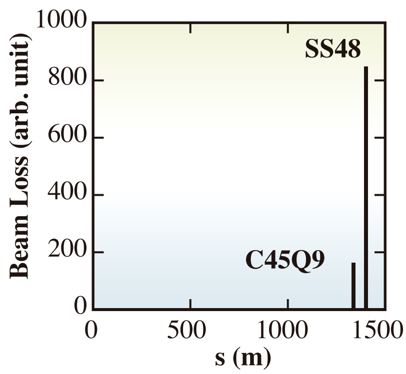

Fig. 11. Tracking result for the case of "beam abort" by CETRA.

Development of Accelerator Diagnostics Beamlines

Beam emittance is one of the most important characteristics of a synchrotron light source. Beam tests of generating short X-ray pulses have been carried out at SPring-8 by decreasing the momentum compaction factor α of the storage ring optics [13]. Operating the ring with optics of lower a value is controversial as it deteriorates the beam emittance.

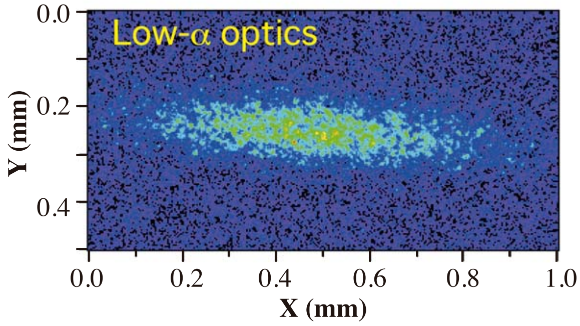

Fig. 12. An example of the beam profile observed with the XBI in the test of low-α operation. The horizontal beam size (s) was 216 mm, and the emittance deduced from the measured beam size was 25 nm·rad, consistent with the designed value of the optics.

Therefore, emittance diagnostics are crucial for tests of low-α operation. Figure 12 shows an example of the beam profile observed with the X-ray beam imager [14] implemented at the diagnostics beamline I (BL38B2). The emittance deduced from the measured beam size was consistent with the designed value, and it was confirmed that the emittance was properly controlled as designed in the tests of low-α operation.

We have plans to develop a diagnostics system of emittance and energy spread of the electron beam by measuring the energy spectrum and angular divergence of the higher harmonics of the ID at the diagnostics beamline II (BL05SS). Since the error magnetic fields reduce the spectral photon flux of higher harmonics, we have elaborated on tuning the magnetic field before installing of the ID. The well-corrected fundamental phase error of the magnetic field has led us to detect clear peaks of higher harmonics in the observed energy spectrum of the ID.

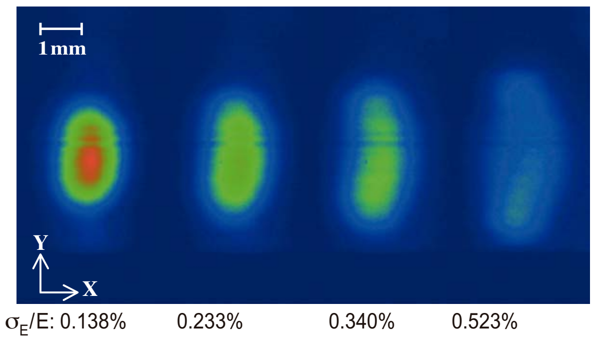

Fig. 13. Observed spatial profiles of the 19th harmonics of the ID at the monochromatic photon energy of 8.3 keV, while modulating the RF phase of the electron beam at the synchrotron frequency of 2.2 kHz. The horizontal angular aperture was limited by the front-end slit at 4 μrad. The values of the effective energy spread shown at the bottom were deduced by observing simultaneously temporal bunch oscillations with a visible light streak camera at the diagnostics beamline I.

The performance of the ID yielding clear higher harmonics peaks has encouraged us to apply it to the energy-spread diagnostics by observing a spatial profile in the vertical of the higher harmonics and to develop a fast turn-by-turn diagnostics system. Before developing the fast system, by observing the 19th harmonics of the ID, we confirmed experimentally that the vertical angular divergence of the higher harmonics has enough sensitivity to the beam energy spread. Figure 13 shows that the observed vertical profiles have larger widths for larger effective energy spread, which was increased by exciting the energy oscillation by modulating the RF phase at the synchrotron frequency.

We have been investigating the characteristics of an X-ray streak camera (X-SC) at the diagnostics beamline II to apply it to the diagnostics of short X-ray pulses generated by decreasing the momentum compaction factor α or by other methods. The temporal resolution of an X-SC is generally dominated by the effect of the energy spread of electrons emitted by the input photocathode. To evaluate it quantitatively, we analyzed the temporal spreads of single X-ray photons, which are the shortest X-ray pulses, on the X-SC image. Beam tests to generate short X-ray pulses are in progress at SPring-8 by slitting X-rays from an electron bunch tilted by a vertical single kick under nonzero chromaticity [8]. Figure 14 shows an example of an X-SC image of short X-ray pulses thus obtained after a half period of synchrotron oscillation from the single kick. The pulse length of 7.4 ps (FWHM) obtained with the kick is about six times shorter than that without the kick [9].

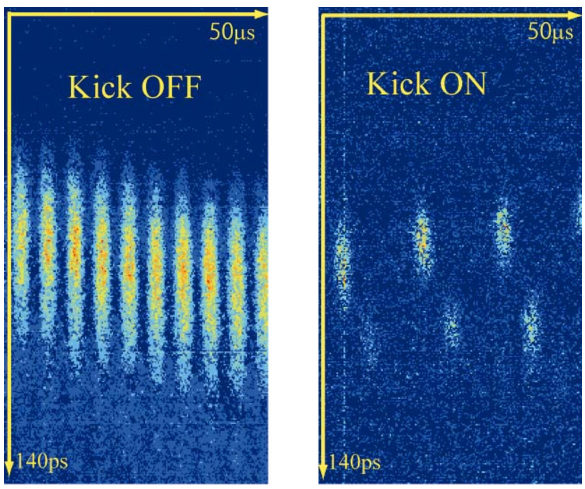

Fig. 14. X-SC image of X-ray pulse with/without a single vertical kick under nonzero vertical chromaticity. The X-SC was operated in the dual-time scan mode, and the horizontal scan separates the pulses from consecutive turns of the stored single bunch.

Investigation of Heating Problem of Gate Valves in the Storage Ring

The SPring-8 storage ring is running with various types of operation mode. Initially, the operation modes were restricted by beam instabilities; however, the limitation was overcome by introducing a bunch-by-bunch feedback system. Now, heat load for finger-type RF shields in gate valves is the major issue behind the restriction. More specifically, the temperatures inside the gate valves are controlled at less than 100°C, taking into account the creep rupture of beryllium-copper (BeCu) of the shields. However, we investigated more precisely the heat mechanism of the gate valves for future upgrades, such as bunch current increase, short pulse beam operation, and so on.

For starters, we assembled a BeCu RF shield with a silver plate, which has high electric conductivity, to suppress heat generation at the RF shield. We installed the gate valve with the silver plated RF shield the storage ring, and measured the temperatures at the RF shield and around it. However, there was no particular change in the temperatures with or without the silver plate on the shield, thus, any effects of the silver plate could not be recognized. This result was quite tricky, and the properties of thermal transfer in the gate valve should be figured out.

Therefore, we performed a bench test to investigate whether the heat load at the RF shield is released around the shield or not. Figure 15 shows a cross section of the gate valve (valve opened). The gate valve has two ICF152 flanges (1) on both sides. Stainless steel parts (2) are fixed with screws on each flange. A BeCu RF shield (3) is fixed between two stainless steel parts ((4) and (5)). In the case of "valve opened", (5) is pressed against (2) by a cam mechanism. There, we suspected that the thermal contact resistance between (2) and (5) is not good. To investigate this issue, we performed the following steps.

First, we mounted a heater on one flange (1) from outside and heated (2) at around 55°C, while keeping (2) and (5) separated. Next, we started to measure temperature changes on (2) and (4) in contact with (2) and (5).

Figure 16 shows measured correlations (marked as black) between time and temperatures on (2) and (4). The thermal contact resistance was calculated as 31.3 K/W. On the other hand, the thermal conductivity of (2) and (4) is 1.9 K/W in the thermal resistance and that the thermal contact resistance is clearly high. Considering the opposite, we concluded that the heat load at the RF shield could not be released enough to surrounding parts and this caused a temperature rise at the RF shield. Furthermore, we improved the gate valve to obtain better contact between (2) and (5), and followed the same test described above (Fig. 16 marked as red). The thermal contact resistance was extracted as 0.9 to 1.4, which is crucially improved by a factor of 1/20 compared with the prior result. In addition, we installed the gate valve, which has improved the contact between (2) and (5), and the maximum temperature rise at the RF shield could be suppressed by 10°C.

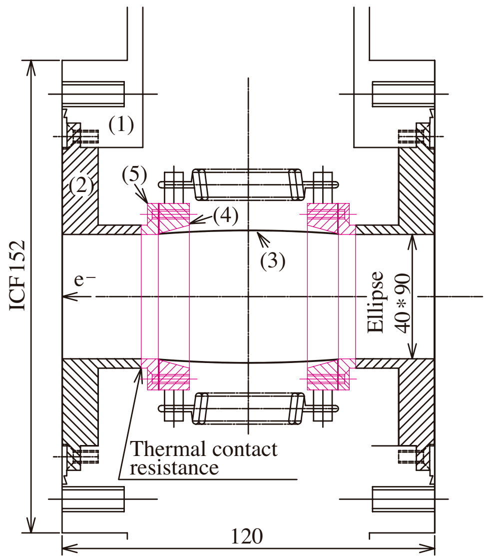

Fig. 15. Cross section of the gate valve (valve opened).

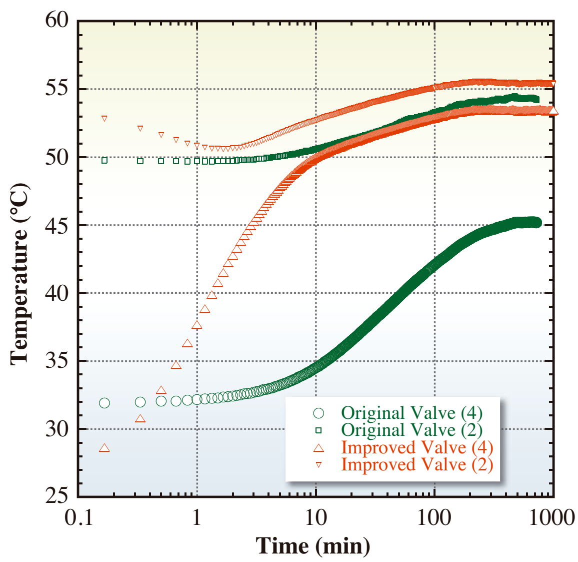

Fig. 16. Measured correlations between time and temperatures on (2) and (4) since the (2) and (5) contact.

Development of an Aluminum Flange with an Electron Beam Modified Seal Edge

Many aluminum (A2219-T852) flanges, which have a knife-edge seal, have been used at the SPring-8 storage ring. Since the flange material is A2219-T852 and ion plated, its delivery time is longer than that of the general-purpose one. Therefore, we investigated the possibility of introducing an aluminum flange that has an electron beam modified (EBM) knife-edge seal. We adopted A5052 as the base material for the EBM flange. Oxygen-free copper is melted in the seal part with the EB welding, and finally, the seal is formed with machining.

We performed an endurance test that consists of 10 times of flange fastening and 3 times of baking (150°C/1 h) for an ICF375 EBM flange prototype. After the endurance test, there was no leak of more than 1×10^{-11} Pa m^3/s and no degradation in the seal edge profile measured using a projector.

Furthermore, component analysis was carried out and the mechanical strength and creep rupture stress were investigated, particularly for the EBM part. It is found that the reformed part has a copper content of ~20 wt% and shows dendritic cells. Its hardness of ~180 Hv is higher than that of the original flange (~130 Hv). On the other hand, the mechanical strength (Table 1) and creep rupture stress (Fig. 17) of the EBM flange are higher than those of the original one in general. However, the elongation of the EBM flange is small, which is similar to that of cast metals.

We confirmed that the EBM flange has sufficient mechanical strength as the original flange at this stage. We plan further investigations on the tolerance to scratch and corrosion and so on.

Table 1. Mechanical properties of A5052-EBM and A2219-T852 at room temperature and 150°C

	Temperature	0.2% proof stress (N/mm^2)	Tensile strength (N/mm^2)	Elongation (%)
A5052-EBM	RT	352	470	0.7
A2219-T852	RT	339	439	8.7
A5052-EBM	150°C	307	444	1.3
A2219-T852	150°C	301	339	18.0

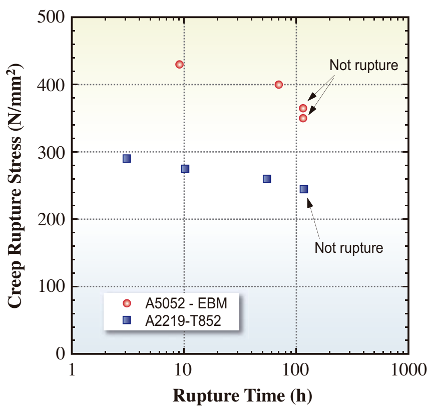

Fig. 17. Measured correlations of creep rupture stress and rupture time of A5052-EBM and A2219-T852 at 150°C.

Research and Development of Femtosecond Pulse X-ray Generation

The generation of an X-ray with an energy of 10.7 keV and a pulse width of 600 fs in two standard deviations can be achieved if we install superconducting crab cavities and a minipole undulator in one of the long straight sections of the SPring-8 storage ring. The flashing repetition of such an X-ray is the same as that of the preexisting synchrotron radiation, or that of the electron bunches circulating around the ring. This feature complements the low repetition of the X-FEL, which has extraordinarily high temporal intensities. This method, in addition, can supply a femtosecond X-ray without causing any disturbance to users on the other beamlines. Its principle of generation [15], performance expected with design parameters [16], and R&D issues such as a high power phase shifter [17] have been described in previous reports.

Now, our technical goal is in sight. Although our plan is not scheduled, it can be pictured more realistically. A layout was drawn to ensure that we could install all the necessary equipment in the building or in the limited open space between the ring and side of the mountain, sitting at the center of the storage ring. Although some existing cooling towers required transfer, we found it possible to construct buildings for a liquid-helium refrigerator and an RF power source (Fig. 18). We also can place four waveguides, four cryostats each with a crab cavity, one liquid helium transfer line, and one gas return line

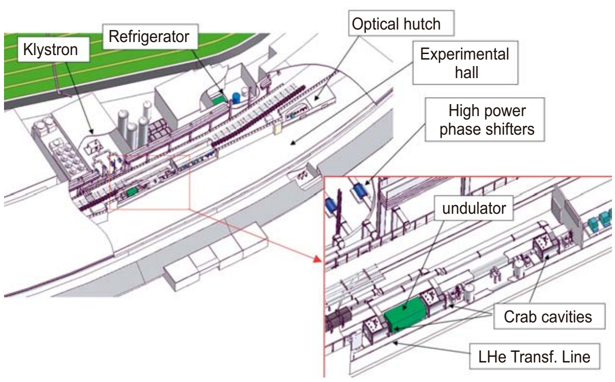

Fig. 18. Layout of the short-pulse X-ray generation system.

in the storage ring tunnel. We chose the route of the waveguides leading from the RF source to the cavities, taking both the phase stability and radiation shielding into account. In the case of a gas leak, the relevant area is partitioned off with bulkheads as a safety measure against oxygen deficiency.

High Power Test of the RF Cavity Dedicated to the Coupler Conditioning

We use 32 single-cell RF cavities in the storage ring and eight 5-cell RF cavities in the booster synchrotron. The resonant frequency of all the cavities is 508.58 MHz. To feed an RF power into the cavities, we used a rectangular-to-coaxial transducing RF input coupler [18]. Since the rated RF power of the 5-cell cavity is 300 kW, we subjected the coupler to a high-power test and conditioned it up to 300 kW before installation in the cavities.

In order to carry out the conditioning efficiently, we developed a compact RF cavity dedicated to the conditioning by referring to the one used in KEK [19]. The cavity has a diameter of 146 mm, a length of 130 mm, and a stub with a diameter of 70 mm and a length of 105 mm. Two couplers facing each other are connected to the cavity and couple to rotational magnetic fields around the stub tightly. An RF power is fed into the cavity through the upstream coupler and extracted from the cavity through the downstream coupler. About 1.7% of the feeding RF power dissipates over the inner surface of the cavity assembly. In order to efficiently remove the heat from the cavity body and prevent the destruction by heat stress, we made the body using OFHC copper and provided it with 13 cooling channels.

The resonant frequency of the cavity assembly inevitably changes because of errors in the measurement for fabricating or assembling. Therefore, we attached a frequency tuner to the cavity. Thus, the VSWR of the cavity assembly is kept less than 1.1 at 508.58 MHz.

We tested the fabricated cavity and conditioned the input couplers. Figure 19 shows the cavity assembly in the RF test stand. The vacuum pressure in the assembly became temporarily worse at about 10^{-2} Pa, but improved to 2×10^{-4} Pa during the conditioning in 20 h. The leakage X-ray from the inside of the cavity was small and we could carry out the high-power test without X-ray shields. Results showed that, we could successfully and stably transmit a rated RF power of 300 kW through the input couplers without damage to the couplers or the cavity.

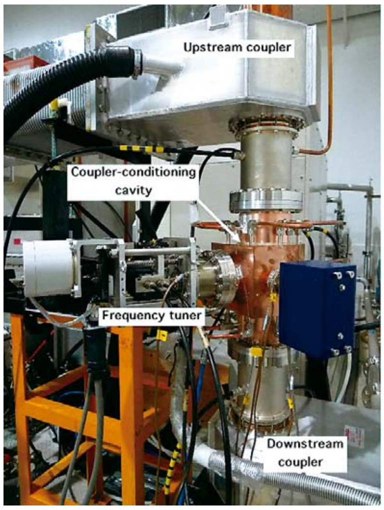

Fig. 19. Cavity assembly in the RF test stand of the SPring-8.

Improvement of RF Tuner Controller of Booster Synchrotron

The booster synchrotron of SPring-8 has 8 RF cavities that are named RF1Cav1···RF1Cav4, RF2Cav1···RF2Cav4, and each cavity consists of 5 cells independently equipped with a tuner controller. These years, it has been observed that the RF reflection occasionally became so large that the interlock system forced the RF supply to turn off. There are a couple of possibilities for the reflection. One is that a discharge occurs somewhere inside, and the other is that a tuner controller, which presumably works as a feedback system for a phase drift, happens to move in an opposite direction.

To solve the above problem, we carefully observed what was happening. For this purpose, we set up a data logger in the low level RF room so that RF phases and reflections at 8 cavities were recorded whenever the above problem occurs. The data logger was triggered by the so-called RF switch that is supposed to turn off when the large RF reflection triggered the interlock system. After observing such an event 16 times, it turned out that twice out of 16 times, the tuner controller moved in the opposite direction, which shifted the RF phase by 16 degrees in 900 ms (Fig. 20(a)). The RF reflection was linearly becoming larger by about 0.5 [arb. unit] in 900 ms, which eventually triggered the RF switch off. In the meantime, the phase drifted by as much as 14 degrees, whereas the tuner controller did not feedback the drift. We attribute it to the malfunction of the tuner controller. The other 14 cases appeared to be caused by discharge somewhere inside, since a

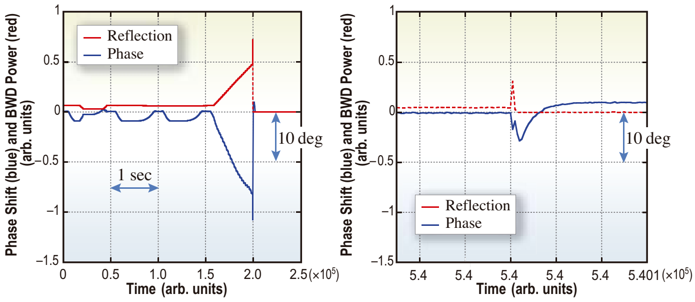

Fig. 20. Two examples of RF reflection and phase measurement.

large RF reflection occurred within a single sampling of the data logger with the sampling rate of 50 kS/s (Fig. 20(b)). Note that the time (horizontal) scales of the two figures are different.

Next, we developed a PLC-based tuner controller. The new controller has several new features, yet is fully compatible with existing apparatus. One of the biggest advantages of the new controller is that by taking advantage of the flexibility of PLC, the relative positions of 5 tuner controllers for each cell in a cavity can be kept constant. The function prevents the 5 tuners from becoming off balance, which that could induce a large RF reflection. Another feature is the availability of the FL-Net connection. In the future, all the connections between VME and PLC will be carried out via the FL-Net. The newly developed tuner controller was at first tested at the RF test stand, where we debugged the PLC logic by operating the controller manually and also remotely. For instance, we remotely operated the tuner controller using our PC to check if the remote commands properly operated the controller. After fixing all the recognized errors at the test stand, the tuner controller was moved to the booster synchrotron and connected to the RF2Cav4 tuner of the booster.

Now, as per November 19, 2009, the booster is running under normal user operation after we reinstalled the new tuner controller to RF2Cav4 in the first week of November, and no problem has been found since then. We made 8 more controllers and replaced all the existing tuner controllers with new ones in the winter of FY 2009. Even if unexpected errors showed up later, we were able to fix them by modifying the PLC software, which is also one of the advantages of PLC-based devices. We will keep watching if the number RF switch off due to the large reflection will be reduced or not.

Power Saving Operation for the SPring-8 Booster Synchrotron

During the top-up operation of the SPring-8 storage ring, the booster synchrotron ejects the beam only when the stored current becomes less than 99.5 mA. The interval of the beam ejection is usually about 20 s. We tested the intermittent excitation of the booster magnets to reduce the power consumption. The magnets stand with DC corresponding to 1 GeV during no beam, and operates 1-8 GeV pattern excitation during beam ejection.

Switching from the continuous to the intermittent operation of the magnet system changes the thermal loading of the equipment and the excitation current. As a result, the betatron tune shifts from the optimum value for the RFKO and it increases the bunch impurity of isolated bunches. Therefore, the intermittent operation was introduced only for a multi-bunch filling pattern without the necessity of bunch purity so far.

We improved a machine cooling system of the utility facility so that the temperature of the main cooling water to be stabilized is constant for both the continuous and intermittent operations. Figure 21 shows a block diagram of the machine cooling system. The temperature control for the main cooling water is performed by adjusting the subsidiary cooling water flow in a heat exchanger. To form the highly purified bunches by the RFKO, the vertical tune-shift should be converged within ±0.002. The improvement of the machine cooling system suppresses the tune-shift to less than 0.0015 between the continuous and intermittent operations. Therefore, the intermittent operation becomes applicable to the filling pattern with several isolated bunches. The results of electrical energy measurement of the magnet system are about 1500 kWh for the continuous operation and about 300 kWh for the intermittent operation. It can be expected

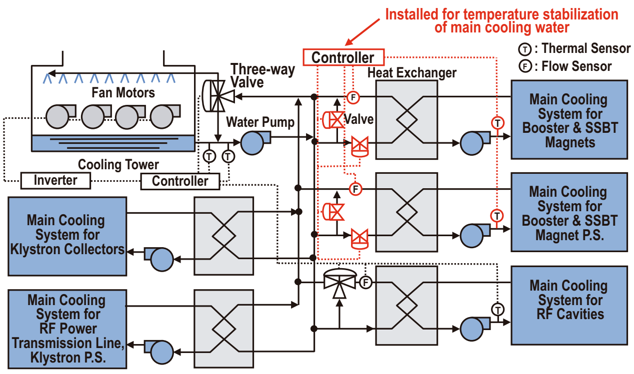

Fig. 21. Block diagram of the machine cooling system of the booster.

that the power consumption of the magnet system of the booster decreases to 1/5 in the top-up operation.

Development of Low Dark Current Accelerating Structure

For several-bunch operation of SPring-8, a very low impurity of bunch filling is required. A major source of the impurity originates from dark currents of an injector linac. An RF knockout system in a booster synchrotron is effectively operated to lower the impurity; however, lower dark currents of the linac are preferable. Thus, we are developing a new accelerating structure to reduce the dark currents emitted from the structure surface. Applied improvements are a new single-feed waveguide coupler and an ellipsoidal cross section of the disk iris. A design view of the structure is shown in Fig. 22.

The source points of the dark current locate near the disk iris where the electric field is concentrated. To moderate this concentration, the shape of the iris cross section was modified from a quasi-circle to an ellipse. The field strength was evaluated using a simulation code, CST Microwave Studio. The maximum field strength is minimized at where the major radius of the ellipse is approximately 4 mm. As a result, the maximum field strength was reduced to 87% of the original shape. The electric-field strength distributions in an original structure and a new one are shown in Fig. 23. Since the field-emitted currents are estimated to be roughly proportional to the electric field to the 16th power, the dark current emitted from the iris will be reduced by an order of magnitude.

In the waveguide coupler, an E-plane of the waveguide is attached to the disk-loaded structure, and the concentration of the surface current becomes smaller than that of a conventional H-field coupler. This feature reduces the pulse heating damage of the structure surface and leads to the reduction of the dark currents.

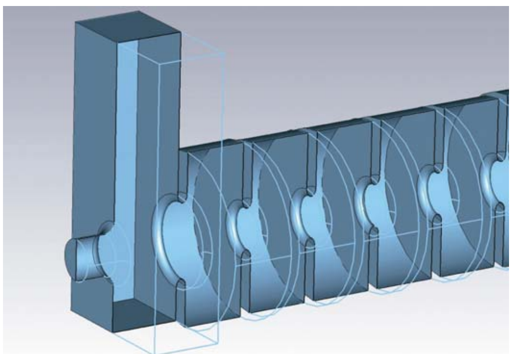

Fig. 22. Design view around the coupler cell of a low dark current accelerating structure.

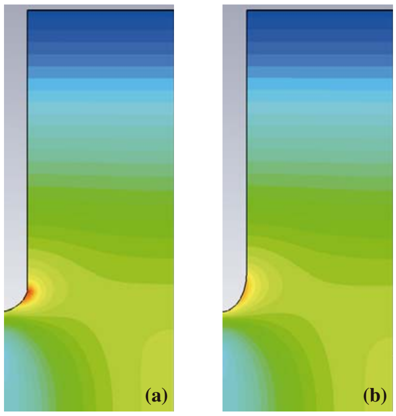

Fig. 23. Electric field strength distribution near the disk-iris. **(a)** existing structure, **(b)** new structure.

After the RF design, a 1-meter-long structure was fabricated as shown in Fig. 24. The main parameters are shown in Table 2. The cavity cells were finished using a diamond turning machine and bonded together by vacuum brazing. We plan a high power test of this structure in 2010.

Fig. 24. Low dark current accelerating structure after brazing.

Table 2. Parameters of low dark current accelerating structure

Frequency	2856 MHz
Phase shift / cell	$2\pi/3$ constant impedance
Coupler type	Waveguide coupler
Iris diameter (2a)	20 mm
Coupler iris diameter	36.4 mm
Disk thickness	5 mm
Iris shape (cross section)	Ellipse
(Major / minor radius)	(4.0 mm / 2.5 mm)
Group velocity v_g/c	0.01
Total length	1050 mm
Filling time	302 ns
VSWR	1.1